Highly Sensitive Coupled Oscillator Based on an Exceptional Point of Degeneracy and Nonlinearity

Alireza Nikzamir and Filippo Capolino[*]
Department of Electrical Engineering and Computer Science, University of California, Irvine, California 92697, USA

We propose a scheme to obtain highly sensitive oscillators in a coupled-resonator system with an exceptional point of degeneracy (EPD) and a small instability. The oscillator with the exceptional degeneracy is realized by using two coupled resonators with an almost balanced small-signal gain and loss, that saturates due to nonlinear effects of the active component, resulting in an oscillation frequency that is very sensitive to a perturbation of the circuit. Two cases are investigated, with two parallel *LC* resonators with balanced small-signal gain and loss that are either coupled wirelessly by mutual inductance or coupled wired by a capacitor. This paper demonstrates theoretically and experimentally the conditions to obtain a second-order EPD oscillator and analyzes the ultrasensitivity of the oscillation frequency to components' perturbation, including the case of asymmetric perturbation that breaks *PT* symmetry. We discuss the effects of nonlinearity on the performance of the oscillator and how the proposed scheme improves the sensing's sensitivity of perturbations. In contrast to previous methods, our proposed degenerate oscillator can sense either positive or negative changes of a circuit component. The degenerate oscillator circuit may find applications in various areas, such as ultrasensitive sensors, tunable oscillators, and modulators.

I. INTRODUCTION

Oscillators are fundamental components of rf electronics. Traditionally, an oscillator is viewed as a positive feedback mechanism utilizing a gain device with a selective reactive circuit. An oscillator generates a continuous, periodic single-frequency output when Barkhausen's criteria are satisfied [1]. The oscillator circuit should have a self-sustaining mechanism such that noise gets filtered, quickly grows and becomes a periodic signal. Most rf oscillators are implemented by only one active device for noise and cost considerations, such as Van der Pol and voltage-controlled oscillators [2]. Oscillators can be realized by a simple *LC* resonator with positive feedback using a negative resistance. Pierce, Colpitts, and tunnel diode oscillators play a role of negative resistance in a circuit, as well as a cross-coupled transistor pair [1,3,4]. All these oscillators are based on a single-pole operation, i.e., a single pole of the system matrix that describes the circuit [1] is rendered unstable when the system is brought above threshold. Oscillators based on an *LC* resonator are the most common type of oscillator, other designs may feature distributed [5–7], ring [8,9], coupled [10], or multimode [11] oscillators, which come with their own challenges and advantages.

In this paper, we discuss the concept of a double-pole oscillator, i.e., an oscillator designed to utilize an exceptional point of degeneracy (EPD) in two coupled resonators, where the degenerate (double) pole is rendered unstable. A system reaches an EPD when at least two eigenmodes coalesce into a single degenerate one, in their eigenfrequencies (eigenvalues) and polarization states (eigenvectors) [12–20]. The letter "*D*" in EPD refers to the key concept of "degeneracy" where the relevant eigenmodes, including the associated eigenvectors are fully degenerate [21]. The degeneracy order refers to the number of coalescing eigenmodes. The concept of EPD has been implemented traditionally in systems made of coupled resonators [22–28], periodic and uniform multimode waveguides [29–33], and also in waveguides using *PT* symmetry [32,34–36]. EPDs have been recently demonstrated also in a temporally periodic single resonator without a gain element [26,37–39], inspired by the finding that EPD exists in spatially periodic lossless waveguides [40–42], resorting to a nondiagonalizability property of the transfer matrix associated to a periodic system.

A very significant feature of a system with EPD is the ultrasensitivity of its eigenvectors and eigenvalues to a perturbation of a system's parameter. This property paves the way to measure a small change in either physical, chemical, or biological parameter that causes a perturbation in the system. Typically, a sensor's sensitivity is related to the amount of spectral shift of a resonance mechanism in

*f.capolino@uci.edu

response to a perturbation in environmental parameters, for example, a glucose concentration or other physical variations like changing pressure, etc. Sensors with EPD can be wired or wirelessly connected to the measuring part of the sensor [43–45]. In principle, higher sensitivity would be enabled with higher orders of degeneracy, such as the more complicated circuit in Ref. [46]. In Refs. [43–46], sensitivity was discussed in the case of symmetric gain and loss. In this paper, we show very high sensitivity of the oscillation frequency to external perturbations of a double-pole oscillator operating at a second-order EPD, focusing on the nonlinear aspects of the implementation.

Based on the general *PT*-symmetry concept [47], *PT*-symmetry circuits have been conceived as two coupled resonators [22,23]. In demonstrating the sensitivity of the responses of these circuits when the circuit is perturbed away from its EPD, *PT* symmetry has been maintained in order to obtain two real-valued frequencies: for example, in Ref. [48], when one side's capacitance is perturbed, the authors tuned the other side's capacitance using a varactor to keep the *PT* symmetry in the circuit, so they can still observe two real-valued shifted frequencies perturbed away from the degenerate EPD frequency. Thus, in previously published schemes (implementing the demonstration of sensitive measurement of a perturbation) the exact value of such a perturbation should be precisely known to tune the other side of the system in order to keep the circuit *PT* symmetric. This seems to contradict the idea that the circuit is used as a sensor of an unknown measurable quantity. That scheme could be saved if combined with an iterative method performing an automatic scan to reconstruct the *PT* symmetry. Anyway, this rebalancing procedure (to keep the system *PT* symmetric) is a further complication for using such a scheme to design a sensor.

A limitation of *PT*-symmetry schemes is that they can detect only perturbations that lead to the same-sign change in a system's component, such as a capacitor's value. This is because a *PT*-symmetric system provides two real-valued frequencies only when the system is perturbed away from its EPD in one direction (for example, for G values smaller than the G_e related to the EPD, when looking at the eigenfrequencies in Fig. 1). If the perturbation makes the system move in the other direction, the shift of the frequencies is in the imaginary parts [22,23,48,49], leading to two complex-valued frequencies and hence to instability. One must also consider that any mismatch between the sensor side (typically the part with losses) and the reader side (typically the part with gain), even involuntary, leads to an asymmetric system. Thus, a *PT*-symmetric system in practice always shows two complex-valued eigenfrequencies and increases the risks of self-sustained oscillations (unless an EPD is designed with a large enough damping factor, larger than the eigenfrequency perturbation due to circuit tolerances). Noise and nonlinearities play a critical role in the robustness of these kinds of applications
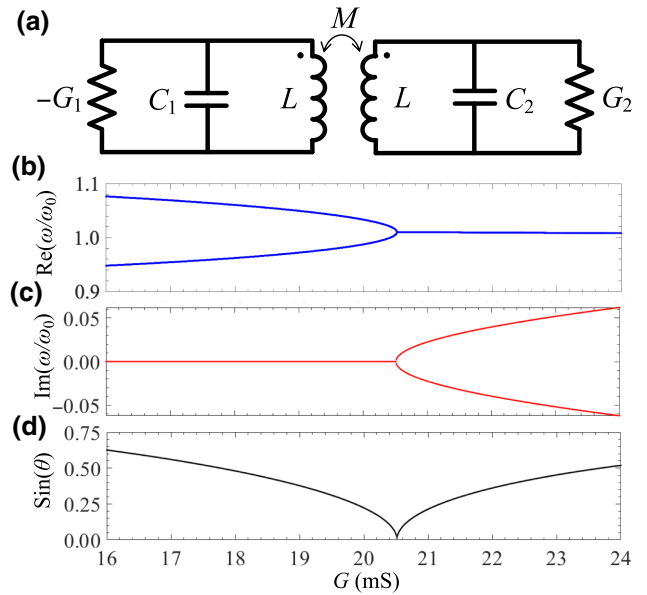
FIG. 1. (a) Coupled resonators terminated with linear $-G_1$ on the gain side ($n = 1$) and G_2 on the loss side ($n = 2$), with $G_1 = G_2 = G$, and inductances $L = 0.1\ \mu$H, mutual coupling $k = M/L = 0.2$, capacitances of $C_n = C_0 = 1$ nF ($n = 1, 2$). The natural frequency of each (uncoupled) LC resonator is $\omega_0 = 1/\sqrt{LC_0} = 10^8\ \text{s}^{-1}$. Normalized eigenfrequencies of the coupled circuit are calculated by using Eqs. (4) and (5). (b) Positive real, and (c) imaginary parts of the resonance angular frequencies normalized by ω_0 varying G on both sides of the EPD value. (d) At the EPD point ($G = G_e = 20.52$ mS, $\omega_e = 1.01 \times 10^8\ \text{s}^{-1}$), two state eigenvectors coalesce demonstrated by the vanishing of $\sin(\theta)$.

and affect the possibility of instability [50]. Some error-correction techniques are studied in Ref. [51] to overcome some of these drawbacks using a nonlinear *PT*-symmetry scheme to enhance the robustness of sensing. A closely related highly sensitivity approach has also been proposed using the concept of white-light cavities that has been then demonstrated to be related to the concept of EPD in *PT*-symmetric systems [52,53].

In this paper, we provide a scheme that starts by using a quasi-*PT*-symmetric condition, working near an EPD, that makes the double-pole system slightly unstable even before having any perturbation. In other words, we turn the above-mentioned practical problems that occur in *PT*-symmetric systems to our advantage when the circuit has to be used in a highly sensitive sensor. We set the gain value slightly higher than the loss counterpart to make the system slightly unstable. As a result of instability and nonlinear gain, the signal grows until the active gain component reaches saturation, and the working operation will be close to the EPD.

We first show the behavior of wirelessly coupled *LC* resonators through the dispersion relation of the resonance

frequency versus perturbation and we discuss the occurrence of EPDs in such a system. In Sec. III, we use the nonlinear model for the gain to achieve the oscillator's characteristics. We show that the oscillation frequency is very close to the EPD frequency. The EPD-based oscillator has an oscillation frequency that is very sensitive to perturbation, exhibiting the typical square-root-like behavior of EPD systems, where the change in frequency of the oscillator is proportional to the square root of the perturbation. In Sec. IV, we demonstrate the highly sensitive behavior of the circuit by breaking *PT* symmetry, i.e., by perturbing the capacitance on the lossy side (the sensing capacitance). In this case, the circuit oscillates at a shifted frequency compared to the EPD one. Notably, both positive and negative perturbations in the capacitance are shown to lead to opposite shifted frequencies, i.e., the proposed scheme detects either positive or negative changes in the capacitance, in contrast to conventional *PT*-symmetry systems [23,24,48] that generate frequency shifts associated to only one sign of the perturbation. The EPD is demonstrated also by analyzing the bifurcation of the dispersion diagram at the EPD frequency by using the Puiseux fractional power-series expansion [16,54]. In Sec. V, we show the condition to have an EPD in two resonators coupled by a capacitor and demonstrate the occurrence of the EPD by using the Puiseux series and experimentally, by using a nonlinear active element. Also, we discuss how noise contributes to the system by showing the power spectrum of the system and the phase noise. The theoretical results are in a good agreement with the experimental results, pointing out that small perturbations in the system can be detected by easily measurable resonance frequency shifts, even in the presence of thermal noise and electronic noise. The advantages of using the proposed circuit as an ultrasensitive sensor and how the experimental results show that the oscillator is sensitive to both positive and negative capacitance changes are discussed in Sec. V. Very sensitive sensors based on the oscillator scheme discussed here can be a crucial part of various medical, industrial, automotive and aerospace applications that require sensing physical, chemical, or biological variations.

II. OSCILLATOR BASED ON COUPLED RESONATORS WITH EPD

We investigate the coupled resonators shown in Fig. 1(a), where one parallel *LC* resonator includes gain (left side, or $n = 1$) and the other includes loss (right side, or $n = 2$). In this ideal circuit, the negative conductance $-G_1$ (gain) has the same magnitude as the loss G_2 to exactly satisfy *PT* symmetry. When a system satisfies *PT* symmetry, it means that the system is invariant to the application of the two operators of parity "*P*" transformation [making a spatial reflection (e.g., $x \rightarrow -x$)], and

time-reversal "*T*" transformation ($t \rightarrow -t$), where x is the coordinate and t is the time.

By writing Kirchhoff's current laws, we obtain the equations

$$
\begin{cases}
\frac{d^2 Q_1}{dt^2} = -\frac{1}{LC_1(1-k^2)}Q_1 + \frac{k}{LC_2(1-k^2)}Q_2 + \frac{G_1}{C_1}\frac{dQ_1}{dt} \\
\frac{d^2 Q_2}{dt^2} = +\frac{k}{LC_1(1-k^2)}Q_1 - \frac{1}{LC_2(1-k^2)}Q_2 - \frac{G_2}{C_2}\frac{dQ_2}{dt}
\end{cases}, \quad (1)
$$

where Q_n is the capacitor charge on the gain side ($n = 1$) and on the lossy side ($n = 2$), and $\dot{Q}_n \equiv dQ_n/dt$ is the current flowing into the capacitor. We define the system's state vector as $\boldsymbol{\Psi}(t) \equiv [Q_1, Q_2, \dot{Q}_1, \dot{Q}_2]^{\mathrm{T}}$, consisting of a combination of stored charges and currents on both sides, and the superscript T denotes the transpose operation. Thus, we describe the system in a Liouvillian formalism as

$$
\frac{d\boldsymbol{\Psi}}{dt} = \underline{\mathbf{M}}\boldsymbol{\Psi},
$$

$$
\underline{\mathbf{M}} = \begin{pmatrix}
0 & 0 & 1 & 0 \\
0 & 0 & 0 & 1 \\
-\frac{1}{LC_1(1-k^2)} & \frac{k}{LC_2(1-k^2)} & \frac{G_1}{C_1} & 0 \\
\frac{k}{LC_1(1-k^2)} & -\frac{1}{LC_2(1-k^2)} & 0 & -\frac{G_2}{C_2}
\end{pmatrix}. \quad (2)
$$

We are interested in finding the eigenfrequencies and eigenvectors of the system matrix $\underline{\mathbf{M}}$. Assuming signals of the form $Q_n \propto e^{j\omega t}$, we write the eigenvalues problem associated with the circuit equations, $(\underline{\mathbf{M}} - j\omega\underline{\mathbf{I}})\boldsymbol{\Psi} = 0$, where $\underline{\mathbf{I}}$ is a 4 by 4 identity matrix. Then, by solving $P(\omega) \triangleq \det(\underline{\mathbf{M}} - j\omega\underline{\mathbf{I}}) = 0$, the four eigenfrequencies are found. By assuming $C_1 = C_2 = C_0$ and linear $G_1 = G_2 = G$, a symmetry condition that has been described as *PT* symmetric [22], the characteristic equation takes the simplified form

$$
P(\omega) = \left(1 - k^2\right)\left(\frac{\omega}{\omega_0}\right)^4 + \left(G^2 Z^2 \left(1 - k^2\right) - 2\right)
$$
$$
\times \left(\frac{\omega}{\omega_0}\right)^2 + 1 = 0, \quad (3)
$$

where $Z = \sqrt{L/C_0}$ is a convenient normalizing impedance, and $\omega_0^2 = 1/(LC_0)$. The characteristic equation is quadratic in ω^2; therefore, ω and $-\omega$ are both solutions. Moreover, the ω's coefficients in the characteristic equation are real, hence ω and ω^* are both solutions, where * represents the complex conjugate operation. The 4 by 4 matrix $\underline{\mathbf{M}}$ results in four angular eigenfrequencies, which are found analytically as

$$
\omega_{1,3} = \pm\omega_0\sqrt{\frac{1}{1-k^2} - \frac{G^2 Z^2}{2} - \sqrt{b}}, \quad (4)
$$

$$\omega_{2,4} = \pm\omega_0\sqrt{\frac{1}{1-k^2} - \frac{G^2Z^2}{2} + \sqrt{b}}, \qquad (5)$$

$$b = -\frac{1}{1-k^2} + \left(\frac{G^2Z^2}{2} - \frac{1}{1-k^2}\right)^2. \qquad (6)$$

Because of the mentioned symmetries of the eigenfrequencies in a realistic system with purely real time-domain signals (e.g., voltages and currents), in the following we focus mainly on the two solutions with positive real part, namely ω_1 and ω_2. The EPD frequency is found when the component values obey the condition

$$b = 0. \qquad (7)$$

So far $b = 0$ is a necessary condition, but in a simple system like this, the eigenvectors can be represented as a function of the eigenvalues so this condition is also sufficient to show the convergence of the eigenvectors, hence for an EPD to occur. Under this condition, we calculate the EPD angular frequency based on Eqs. (4), (5) and (7) as $\omega_1 = \omega_2 = \omega_e$, where

$$\omega_e = \frac{\omega_0}{\sqrt[4]{1-k^2}}. \qquad (8)$$

Only the two eigenfrequencies with positive-real part, namely ω_1 and ω_2, are shown in Figs. 1(b) and 1(c) varying G. It is seen from this plot that the system's eigenfrequencies are coalescing at a specific balanced linear gain and loss value $G = G_e$, where $b = 0$. Note that in this scenario, the EPD-enabling value G_e is derived from Eq. (7) as

$$G_e = \frac{1}{Z}\left(\frac{1}{\sqrt{1-k}} - \frac{1}{\sqrt{1+k}}\right). \qquad (9)$$

For clarification, when $G = 0$ (lossless and gainless circuit), we have two pairs of resonance frequencies $\omega_{1,3} = \pm\omega_0/\sqrt{1+k}$ and $\omega_{2,4} = \pm\omega_0/\sqrt{1-k}$, and $\omega_1 \neq \omega_2$ always, except for the trivial case with $k = 0$, when these eigenfrequencies are equal to those of the isolated circuits, but since the two circuits are isolated this is not an important degeneracy. With the given values of L and C in the caption of Fig. 1, a second-order EPD occurs when $G = G_e = 20.52$ mS. In this case, the circuit's currents and charges grow linearly with increasing time as $Q_n \propto te^{j\omega_e t}$, and they oscillate at the degenerate frequency ω_e. Also, when perturbing G near the EPD point, the eigenfrequencies have a square-root-like behavior as $|\omega - \omega_e| \propto \pm\sqrt{(GZ)^2 - (G_eZ)^2}$ [23]. A second coalescence (i.e., degeneracy) happens for larger values of G, i.e., at $G'_e = (1/Z)\left[1/\sqrt{1-k} + 1/\sqrt{1+k}\right]$. However, when $G > G'_e$ all eigenfrequencies are purely imaginary, so we study only cases with $G < G'_e$, discussed next. In the strong

coupling regime, $0 < G < G_e$, the eigenfrequencies are purely real, and the oscillation wave has two fundamental frequencies. In the weak coupling regime, $G_e < G < G'_e$, the frequencies are complex conjugate and the imaginary part of the angular eigenfrequencies is nonzero, and it causes two system solutions (Q_1 and Q_2) with damping and exponentially growing signals in the system. Since the solution of the circuit is $Q_n \propto e^{j\omega t}$, the eigenfrequency with a negative imaginary part is associated to an exponentially growing signal and the oscillation frequency is associated to the real part of the eigenfrequency.

At each positive (real part) angular eigenfrequency ω_1 and ω_2, calculated by Eqs. (4) and (5), we find the two associated eigenvectors $\mathbf{\Psi_1}$ and $\mathbf{\Psi_2}$ by using Eq. (2). A sufficient condition for an EPD to occur is that at least two eigenvectors coalesce, and that is what we check in the following. Various choices could be made to measure the state vectors' coalescence at an EPD, and here, the "Hermitian angle" between the state amplitude vectors $\mathbf{\Psi_1}$ and $\mathbf{\Psi_2}$ is defined as [55]

$$\theta = \arccos\left(\frac{|\langle\mathbf{\Psi_1}, \mathbf{\Psi_2}\rangle|}{||\mathbf{\Psi_1}||\,||\mathbf{\Psi_2}||}\right). \qquad (10)$$

Here, the inner product is defined as $\langle\mathbf{\Psi_1}, \mathbf{\Psi_2}\rangle = \mathbf{\Psi_1}^\dagger\mathbf{\Psi_2}$, where the dagger symbol † denotes the complex conjugate transpose operation, $||$ represents the absolute value, and $||\,||$ represents the norm of a vector. According to this definition, the state vectors $\mathbf{\Psi_1}$ and $\mathbf{\Psi_2}$ correspond to resonance frequencies ω_1 and ω_2, respectively. When some system's parameter is varied, eigenfrequencies and associated eigenvectors are calculated using Eq. (2). In the case when G varies, Fig. 1(d) shows that the sine of the angle θ between the two eigenvectors vanishes when the eigenfrequencies coalesce, which indicates the coalescence of the two eigenmodes in their eigenvalues and eigenvectors and hence the occurrence of a second-order EPD.

III. OSCILLATOR CHARACTERISTICS

This section describes the features of a double-pole (degenerate) oscillator made of two coupled resonators with discrete (lumped) elements with balanced gain and loss, coupled wirelessly by a mutual inductance as in Fig. 1. The transient time domain, frequency spectrum, and double pole (or zero, depending on what we look at) features are discussed. A cubic model (nonlinear) of the active component providing gain is considered. The parameters used here are the same as those used in the previous section, where $G_e = 20.52$ mS leads to an EPD of order two at a frequency of 16.1 MHz, except that here $-G_1$ accounts also for the nonlinear part responsible for the saturation effect.

A. Transient and frequency behavior

Time- and frequency-domain responses of the coupled resonators circuit are obtained by using the Keysight Advanced Design System (ADS) circuit time-domain simulator, as shown in Figs. 2(b)–2(d). The cubic model for gain, in Fig. 2(a), represented as

$$i = -G_1 v + \alpha v^3 \qquad (11)$$

is a simplified description of the gain obtained from a cross-coupled transistor pair or an operational amplifier (opamp) based circuit. Here, $-G_1$ is the small-signal gain provided by the negative slope of the $i - v$ curve, i.e., is the negative conductance in the small-signal region, and $\alpha = G_1 / (3V_b^2)$ is a third-order nonlinearity that describes saturation, where V_b is the turning point voltage determined by the biasing dc voltage. We assume $V_b = 1$ V, and to start self-sustained oscillation, we assume that gain $-G_1$ is not a perfect balance of the loss G_2. Indeed, we assume that G_1 is 0.1% larger than G_2. Therefore, the system is slightly perturbed away from the PT-symmetry condition to start with. We also assume white noise (at the temperature of 298 K) is present in the loss resistor and it is indeed the initial condition for starting oscillations. The slightly broken small-signal gain and loss symmetry causes an eigenfrequency to have a slightly negative imaginary part. The signals in the system are in the form of $e^{j\omega t}$ and even a small negative imaginary part of an eigenfrequency makes the system unstable because the system's signal grows. Therefore, the system starts oscillating at a frequency associated to the eigenfrequency with a negative imaginary part; then, such a frequency is slightly perturbed because of the nonlinear saturation effect.

Therefore, because $G_1 = G_2(1 + 0.001)$ the circuit is slightly unstable and starts oscillations; after a transient, the circuit saturates, yielding a stable oscillation, as shown in Figs. 2(b)–2(d). As shown in Figs. 1(b) and 1(c) assuming linear gain, for values of $G_1 = G_2 < G_e$, the system has two distinct eigenfrequencies ω_1 and ω_2 with zero imaginary part. However, when using the cubic nonlinear model with $G_1 = 1.001G_2$, with $G_2 \lesssim G_1 < G_e$, the imaginary part is not zero anymore because of the slightly broken PT symmetry. Thus, when using the cubic model, after an initial transient, the oscillation signal associated to the eigenfrequency with a negative imaginary part dominates and makes the system saturate. Considering again the initial result in Figs. 1(b) and 1(c) assuming linear gain, it is noted that when $G_1 = G_2 > G_e$, we have two complex conjugate eigenfrequencies, and the one associated to the negative imaginary part makes the circuit oscillate. However, when using the cubic gain model with $G_1 = 1.001G_2$, with $G_1 \gtrsim G_2 > G_e$, eigenfrequencies approximately follow the linear gain eigenfrequency trend. It means that for the values $G_1 \gtrsim G_2 > G_e$, we have a larger negative imaginary part of the eigenfrequency than when $G_2 \lesssim G_1 \le G_e$.
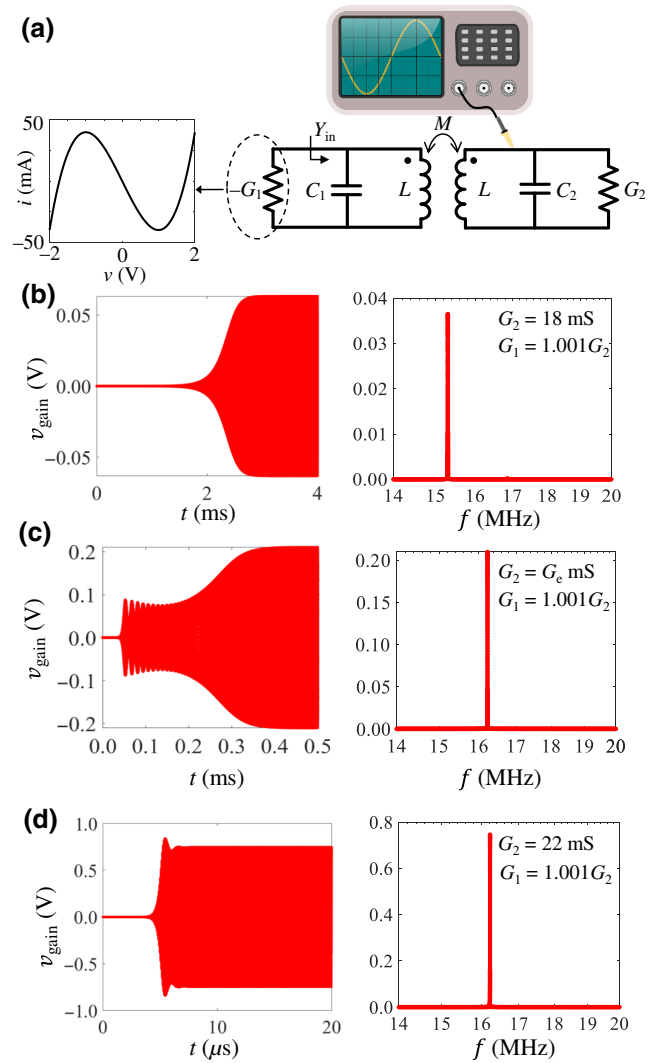
FIG. 2. (a) Cubic gain $i - v$ curve with parameters $G_1 = G_e = 20.52$ mS and $\alpha = 6.84$ mS/V^2 (it corresponds to $V_b = 1$ V). Time-domain response and frequency spectrum of the oscillatory signal with a cubic model where the gain is always 0.1% more than the loss (i.e., $G_1 = 1.001G_2$) with: (b) $G_2 \lesssim G_1 < G_e$, (c) $G_1 = 1.001G_e$ and $G_2 = G_e$, and (d) $G_1 \gtrsim G_2 > G_e$, where $G_e = 20.52$ mS.

The rising time is related to the magnitude of the negative imaginary part of the eigenfrequency; indeed, as shown in Figs. 2(b)–2(d), the rising time is different in the three cases. By going further from the EPD point, the signal saturates in a shorter time. In all cases, the frequency spectrum of the time-domain signal is found by taking the Fourier transform of the voltage on the gain side after reaching saturation, for a time window of 10^3 periods.

B. Root locus of zeros of the total admittance

This subsection discusses the frequency (phasor) approach to better understand the degenerate resonance

frequencies of the coupled resonators' circuit. We use the admittance resonance method and we demonstrate the occurrence of double zeros at the EPD. The resonance condition based on the vanishing of the total admittance implies that

$$Y_{\text{in}}(\omega) - G_1$$

$$= \frac{P(\omega)}{j\left(L/\omega_0^2\right)\left(1-k^2\right)\omega^3 + L^2 G_1 \left(1-k^2\right)\omega^2 - jL\omega} = 0,$$

$$(12)$$

where the Y_{in} is the input admittance of the linear circuit, including the capacitor C_1, looking right as shown in Fig. 2(a). Here, we assume linear gain with $G_1 = G_2 = G$, i.e., satisfying *PT* symmetry.

The polynomial $P(\omega)$ is given in Eq. (3). We calculate the eigenfrequencies by finding the zeros of $Y_{\text{in}}(\omega) - G$, and this leads to the same ω zeros of $P(\omega) = \det(\underline{\mathbf{M}} - j\omega\underline{\mathbf{I}}) = 0$. Note that $\omega(G)$ and $-\omega(G)$ are both solutions of Eq. (12), as well as both $\omega(G)$ and $\omega^*(G)$. The trajectories of the zeros of this equation, i.e., the resonance frequencies $\omega(G)$, are shown in Fig. 3 by varying linear G from 18 mS to $G = 22$ mS (we recall that in this case $G = G_1 = G_2$), in the complex frequency plane. We show only the roots with $\text{Re}(\omega) > 0$ for simplicity. At the EPD occurring when $G = G_e = 20.52$ mS, the two ω solutions coincide, and the above equation reduces to $Y_{\text{in}}(\omega) - G_e \propto (\omega - \omega_e)^2$, i.e., the admittance exhibits a double zero at the EPD angular frequency ω_e. This unique property is also responsible for the square-root-like behavior of resonance frequency variation due to the perturbation in a system, as discussed next, which is the key to high sensitivity. Moreover, for values $G < G_e$, the two resonance frequencies are purely real, and for $G > G_e$, the two resonance frequencies are a complex conjugate pair.

IV. SENSOR POINT OF VIEW

A. High sensitivity and the Puiseux fractional power expansion

As mentioned in the Introduction, when the system operates at an EPD, the eigenfrequencies are extremely sensitive to system perturbations. This property is intrinsically related to the Puiseux series [54] that provides a fractional power-series expansion of the eigenvalues in the vicinity of the EPD point. We consider a small relative perturbation

$$\Delta_X = \frac{X - X_e}{X_e}, \qquad (13)$$

where X is the perturbated value of a system's element, and X_e is the unperturbed value that provides the EPD of second order. A perturbation Δ_X leads to a perturbed
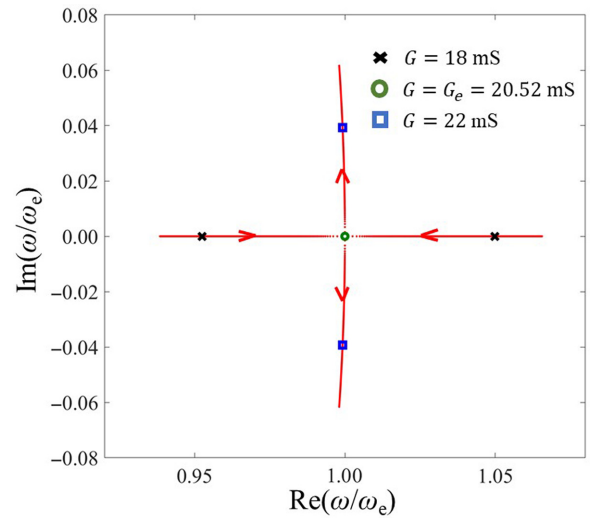
FIG. 3. The trajectories of the zeros of $Y_{\text{in}}(\omega) - G = 0$ show the two resonance frequencies when varying G from 15 to 25 mS (we assume linear gain with $G_1 = G_2 = G$). When $G = G_e$, the two branches meet at ω_e. Therefore, at the EPD, the frequency ω_e is a double zero of $Y_{\text{in}}(\omega) - G_e = 0$. We plot only the trajectories of the two eigenfrequencies with positive real part.

matrix $\underline{\mathbf{M}}(\Delta_X)$ and, as a consequence, it leads to two distinct perturbed eigenfrequencies $\omega_p(\Delta_X)$, with $p = 1, 2$, near the EPD eigenfrequency ω_e as predicted by the Puiseux series containing power terms of $\Delta_X^{1/2}$. Accordingly, a good approximation of the two $\omega_p(\Delta_X)$, with $p = 1, 2$, is given by the first-order expansion

$$\omega_p(\Delta_X) \simeq \omega_e + (-1)^p \alpha_1 \sqrt{\Delta_X}. \qquad (14)$$

Following Refs. [16,54], we calculate α_1 as

$$\alpha_1 = \sqrt{-\frac{[\partial H(\Delta_X, \omega)/\partial\Delta_X]}{(1/2!)[\partial^2 H(\Delta_X, \omega)/\partial\omega^2]}}, \qquad (15)$$

where $H(\Delta, \omega) = \det[\underline{\mathbf{M}}(\Delta) - j\omega\underline{\mathbf{I}}]$ and its derivatives are evaluated at the EPD, i.e., at $\Delta_X = 0$ and $\omega = \omega_e$.

Consider a coupled *LC* resonator, as described in Fig. 2(a), assume the capacitor C_2 on the lossy side is perturbed from the initial value as $(1 + \Delta_{C_2})C_e$, where C_e is the unperturbed value for both C_1 and C_2: the coefficient α_1 is found analytically as

$$\alpha_1 = \sqrt{\frac{L^2\omega_e^2 G_e^2 \left[1 + (C_e\omega_e/G_e)\right]\left(1-k^2\right) + \left(1 - C_e L\omega_e^2\right)}{L^2\left(6C_e^2\omega_e^2 + G_e^2\right)\left(1-k^2\right) - 2C_e L}}.$$

$$(16)$$

The Puiseux fractional power-series expansion, Eq. (14), indicates that for a small perturbation such that $|\Delta_X| \ll 1$,

the eigenfrequencies change dramatically from their original degenerate value due to the square-root function. The Puiseux series first-order coefficient is evaluated by Eq. (16) as $\alpha_1 = 10^7(1.693 + j\,1.530)$ rad/s. The coefficient α_1 is a complex number implying that the system always has two complex eigenfrequencies, for any C_2 value. In Figs. 4(a) and 4(b), the estimate of ω_p, with $p = 1, 2$, using the Puiseux series is shown by a dashed black line. The calculated eigenfrequencies by directly solving the characteristic equation, Eq. (3), are shown by solid blue and red lines, representing unstable and stable solutions, respectively. In this example, C_2 is the sensing capacitance to detect possible variations in chemical or physical parameters, transformed into electrical parameters, like the frequency of oscillation in the circuit. For a small value of Δ_{C_2}, around the EPD value $\Delta_{C_2} = 0$, the imaginary and real parts of the eigenfrequencies experience a sharp change, resulting in a very large shift in the oscillation frequency. Note that this rapid change in the oscillation frequency is valid for both positive and negative changes of Δ_{C_2}, which can be useful for various sensing applications. Note also that a perturbation of PT symmetry led to instability.

To show how the telemetric sensor with nonlinearity works, we now consider that the gain element is nonlinear, following the cubic model in Eq. (11), where the small-signal negative conductance is $-G_1$, with value $G_1 = 1.001G_e$, i.e., increased by 0.1% from its loss balanced value G_e, as discussed earlier, to make the circuit slightly unstable and start self-oscillations. The capacitor C_2 on the lossy side is perturbed by $\pm 0.5\%$ steps and we perform time-domain simulations using the circuit simulator implemented in the Keysight ADS circuit simulator. Noise is assumed in the lossy element G_2 to start oscillations. The time-domain voltage signal at the capacitor C_1 on the gain side is read, and then, we take the Fourier transform of such signal, after reaching saturation, for a time window of 10^3 periods. The oscillation frequency evolution by changing Δ_{C_2} is shown in Fig. 4 by green dots. There is no imaginary part of the frequency associated to such a signal since it is saturated and steady, and the time-domain signal has the shape of an almost pure sinusoid after reaching saturation (phase noise is discussed later on in this paper). The oscillation frequency curve dispersion (green dots) still has a square-root-like shape of the perturbation.

To show how the sensitivity is improved when using the second-order EPD (double-pole) oscillator, we compare its sensitivity to an analogous scheme made of one single LC resonator, with an inductance of $L = 0.1\ \mu$H and capacitance of $C_2 = 1$ nF (same values as in the case of coupled LC circuits) without adding gain or loss. The resonance frequency of the LC resonator is $f_0 = 1/(2\pi\sqrt{LC_2})$ and by perturbing the capacitance C_2, the resonance frequency changes as $f \approx f_0(1 - \Delta_{C_2}/2)$. Figure (4)(c) shows the comparison between two cases: (i) oscillation frequency of
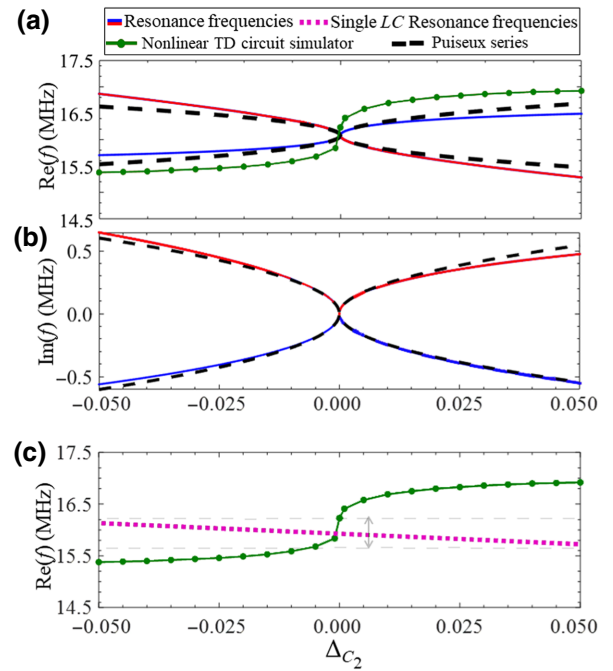
FIG. 4. High sensitivity of the circuit to a variation of capacitance C_2. We show the (a) positive-real and (b) imaginary parts of the resonance frequencies (using linear gain) when varying C_2, compared to the frequency of oscillation after saturation when using nonlinear gain. Solid blue and red lines show the resonance frequencies obtained by solving the characteristic equation, Eq. (3); dashed lines show the estimate obtained by using the Puiseux fractional power-series expansion truncated to its first order. In both cases, gain is a linear negative conductance with $G_1 = G_2 = G_e$. Green dots in (a) show the oscillation frequencies using nonlinear gain; results are obtained by using the time-domain circuit simulator Keysight ADS using the small-signal negative conductance $-G_1$ with $G_1 = 1.001G_e$, i.e., it is increased by 0.1% from its loss balanced value G_e (we recall that $G_2 = G_e$). The frequencies of oscillation are obtained by applying a Fourier transform of the capacitor C_1 voltage after the system reaches saturation, for each considered value of C_2. (c) Sensitivity comparison with single linear LC resonator, when varying Δ_{C_2}. The much higher sensitivity of the EPD oscillator with double pole is clear. Note that the whole frequency variation relative to the full perturbation range of capacitance $(-5\% < \Delta_{C_2} < 5\%)$ for the single LC resonator could be achieved by only $1/10$ of the perturbation $(-0.5\% < \Delta_{C_2} < 0.5\%)$ when the EPD-based circuit is used. The highest sensitivity of the EPD circuit is shown for very small perturbations Δ_{C_2}.

the EPD-based oscillator with nonlinear gain (green dots) using the time-domain circuit simulator Keysight ADS, and (ii) the resonance frequency of the single LC resonator (dashed pink). The results demonstrate that the EPD-based circuit with nonlinearity has higher sensitivity (square-root-like behavior due to the perturbation) than a single-LC resonator without EPD (linear behavior). The whole frequency variation, relative to the full perturbation range
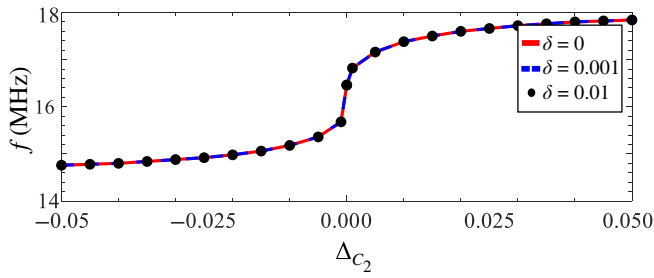
FIG. 5. Robustness of the high sensitivity of the circuit to a variation of capacitance C_2. The oscillator's fundamental frequencies of the circuit after each 0.5% perturbation on C_2 by using nonlinear gain are shown here, considering three values of gain $G_1 = G_e(1 + \delta)$, where $G_2 = G_e$, for three different values of $\delta = 0, 0.001$, and 0.01. These three plots are on top of each other, meaning that even with a 1% mismatch between gain and loss, the oscillator's fundamental frequencies are the same as those for smaller unbalanced situations. It is worthwhile to note that both positive and negative perturbations of C_2 are detected.

of capacitance ($-5\% < \Delta_{C_2} < 5\%$) for the single LC resonator, could be achieved by only 1/10 of the perturbation ($-0.5\% < \Delta_{C_2} < 0.5\%$) when the EPD-based circuit is used. The highest sensitivity of the EPD circuit is shown for very small perturbations Δ_{C_2}, e.g., $|\Delta_{C_2}| \approx 1\%$. For larger Δ_{C_2} variations, i.e., around $|\Delta_{C_2}| \approx 5\%$, the slope of the flattened square-root-like curve is similar to the slope of the curve relative to the perturbed LC resonator.

Figure 5 shows another aspect, the flexibility in choosing the gain value in the nonlinear circuit, i.e., different levels of mismatch between gain and loss, using different values for the small-signal negative conductance $G_1 = G_e(1 + \delta)$ where $\delta = 0, 0.001$, and 0.01 represent the mismatch between the loss and gain side (we recall that $G_2 = G_e$). As shown in Fig. 5, even with 1% mismatch between gain and loss, the nonlinear circuit shows the same behavior in the perturbation of the oscillation frequency, that is even matched to the case with $\delta = 0$. Thus, working in the unstable oscillation configuration using nonlinearity in the coupled circuit gives us the freedom to loosely tune the gain component's value and it works well even with some mismatch between gain and loss.

The oscillation frequency is highly sensitive to the capacitance perturbation on either side of the circuit, either on the loss or gain side. Though not shown explicitly, we observe this feature theoretically, by calculating the eigenfrequencies from $\det(\underline{\mathbf{M}} - j\omega\mathbf{I}) = 0$ when varying C_1, and also verify the shifted resonance frequencies using the prediction provided by the Puiseux series. Also, we observe in time-domain analyses with Keysight ADS circuit simulators using nonlinear gain, that the shift of the oscillation frequency is more sensitive to perturbation of C_1 than C_2. In this paper, however, we show only the result from
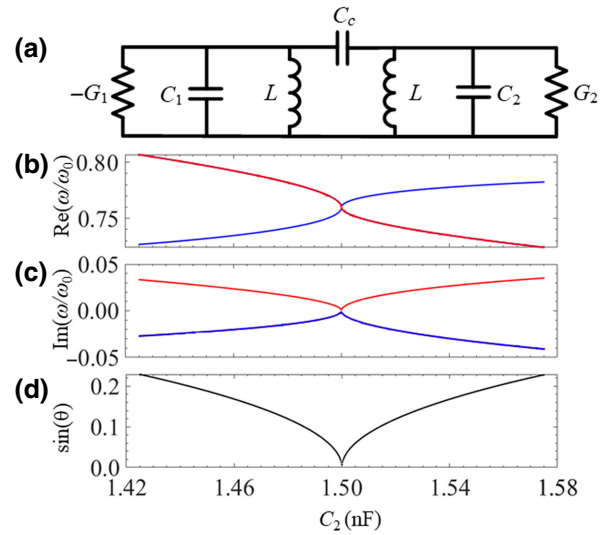
FIG. 6. (a) Coupled resonators terminated with gain $-G_1$ and loss G_2, with $G_1 = G_2 = G_e = 9$ mS, and $L = 10\ \mu$H, coupling capacitance $C_c = 1.5$ nF, capacitances $C_1 = C_2 = C_e = 1.5$ nF. These parameters lead to an EPD. The isolated (i.e., without coupling) resonance frequency of each LC resonator is $\omega_0 = 1/\sqrt{LC_e} = 25.8 \times 10^6$ s^{-1}. The eigenfrequencies of the coupled circuit are calculated by solving $\det(\underline{\mathbf{M}} - j\omega\mathbf{I}) = 0$. (b) Positive-real and (c) imaginary parts of the angular eigenfrequencies normalized by ω_0, varying C_2 around the EPD value C_e. Blue and red solid lines represent the unstable and stable eigenfrequency solutions, respectively. (d) At the EPD, the coalescence parameter $\sin(\theta)$ vanishes, indicating that the two state vectors coalesce.

perturbing C_2 because we want to investigate how a telemetric sensor works (i.e., the sensing capacitance is on the passive part of the coupled resonators' circuit).

V. EXPERIMENTAL DEMONSTRATION OF HIGH SENSITIVITY: CASE WITH COUPLING CAPACITANCE

An analogous system with the properties highlighted in the previous sections is made by the two resonators with balanced gain and loss (PT symmetry) coupled by a capacitor C_c as shown in Fig. 6. Note that in this case the sensing part is capacitor wired to the active part, whereas in the previous circuit the sensing part is connected without wires; both circuits are relevant in applications. In the following, we discuss the condition to have an EPD in this configuration with coupling capacitance and demonstrate the high sensitivity theoretically and experimentally.

First, we find the EPD condition by writing down Kirchhoff's laws and using the Liouvillian formalism using the system vector $\mathbf{\Psi} = [Q_1, Q_2, \dot{Q}_1, \dot{Q}_2]^{\mathrm{T}}$, where Q_n is the capacitor charge on the gain side ($n = 1$) and the lossy side

($n = 2$), and $\dot{Q}_n = dQ_n/dt$, leading to

$$\frac{d\mathbf{\Psi}}{dt} = \underline{\mathbf{M}}\mathbf{\Psi}$$

$$\underline{\mathbf{M}} = \frac{1}{A} \begin{pmatrix} 0 & 0 & A & 0 \\ 0 & 0 & 0 & A \\ -\frac{B_2}{LC_1} & -\frac{C_c}{LC_2^2} & \frac{GB_2}{C_1} & -\frac{GC_c}{C_2^2} \\ -\frac{C_c}{LC_1^2} & -\frac{B_1}{LC_2} & \frac{GC_c}{C_1^2} & -\frac{GB_1}{C_2} \end{pmatrix}$$

$$A = 1 + \frac{C_c}{C_1} + \frac{C_c}{C_2}, \quad B_1 = 1 + \frac{C_c}{C_1}, \quad B_2 = 1 + \frac{C_c}{C_2}.$$

$$\tag{17}$$

In this configuration, EPD occurs at $C_1 = C_2 = C_c = C_e = 1.5$ nF, linear gain and loss $G_1 = G_2 = G_e = 9$ mS, $L = 10$ μH. Figures 6(b) and 6(c) show the positive-real and imaginary parts of the eigenfrequencies when perturbing C_2, calculated by solving for ω the dispersion equation $\det(\underline{\mathbf{M}} - j\omega\mathbf{I}) = 0$, and Fig. 6(d) demonstrates the convergence of eigenvectors at $C_2 = C_e$, hence demonstrating the EPD existence. The eigenfrequency shown with a solid blue line, with negative imaginary part, represents the unstable solution that determines the oscillation frequency. The coalescence of two eigenvectors is observed by defining the angle between them as in Eq. (10), and this indicates the coalescence of the two eigenmodes in their eigenvalues and eigenvectors, and hence the occurrence of a second-order EPD. It is seen from this plot that the system eigenfrequencies are coalescing at a specific capacitance $C_2 = C_e$. The system is unstable for any $C_2 \neq C_e$ because of broken PT symmetry, since there is always an eigenfrequency with $\text{Im}(\omega) < 0$ (blue curve). Moreover, the bifurcation of the dispersion diagram at the EPD is in agreement with the one provided by the Puiseux fractional power-series expansion truncated to its first order, represented by a dashed black line in Fig. 7. The Puiseux series coefficient is calculated as $\alpha_1 = 1.084 \times 10^6 + j\,1.43 \times 10^6$ rad/s by using Eq. (15), assuming negative *linear* gain. The coefficient α_1 is a complex number that implies that the system always has two complex eigenfrequencies, for any C_2 value; that results in an unstable circuit, since one eigenfrequency has $\text{Im}(\omega) < 0$, for any C_2 value.

In order to confirm *experimentally* the high sensitivity to a perturbation in the proposed oscillator scheme based on nonlinear negative conductance (nonlinear gain), the gain is now realized using an opamp (Analog Devices Inc., model ADA4817) whose gain is tuned with a resistance trimmer (Bourns Inc., model 3252W-1-501LF) to reach the proper small-signal gain value of $-G_1 = -9$ mS. Note that we assume that the nonlinear gain is a bit larger (around 0.1%) than the loss on the other side of the circuit to make the system slightly unstable. In the experiment, all the other parameters are as in the previous simulation example: a linear conductance of $G_2 =$
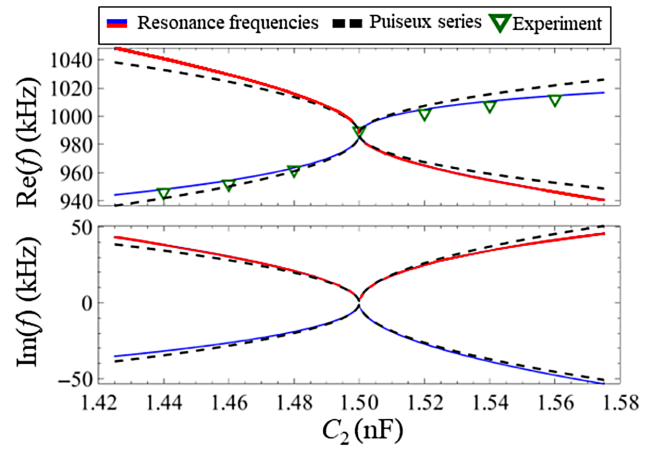
FIG. 7. Experimental proof of exceptional sensitivity. (a) Experimental and theoretical changes in the real part of the resonance frequencies f due to a positive and negative relative perturbation Δ_{C_2} applied to the capacitance C_2 as $(1 + \Delta_{C_2})C_e$. Solid blue and red lines represent the unstable and stable eigenfrequency solutions, respectively. Eigenfrequencies are calculated by finding the zeros of the dispersion equation $\det(\underline{\mathbf{M}} - j\omega\mathbf{I}) = 0$ using linear gain $G_1 = G_2 = G_e = 9$ mS. Dashed black: an estimate using the Puiseux fractional power expansion truncated to its first order, using linear gain. Green triangles: oscillation frequency measured experimentally (using nonlinear gain) after reaching saturation for different values of C_2. The measured oscillation frequency significantly departs from the EPD frequency $f_e = 988.6$ kHz even for a very small variation of the capacitance, approximately following the fractional power expansion $f(\Delta_{C_2}) - f_e \propto \text{Sgn}(\Delta_{C_2})\sqrt{|\Delta_{C_2}|}$. Note that both positive and negative capacitance perturbations are measured.

9 mS, capacitors of $C_1 = C_2 = C_c = 1.5$ nF, and inductors of $L = 10$ μH (Coilcraft, model MSS7348-103MEC). This nonlinear circuit oscillates at the EPD frequency. The actual experimental circuit differs from the ideal simulations using nonlinear gain only in a couple of points: First, extra losses are present in the reactive components associated with their quality factor. The inductor has the lowest quality factor in this circuit with an internal dc resistance of 45 mΩ, from its datasheet, which is however small. Second, electronic components have tolerances. To overcome some of the imperfections in the experiment process, we use a capacitance trimmer (Sprague-Goodman, model GMC40300) and a resistance trimmer in our printed circuit board (PCB) to tune the circuit to operate at the EPD. Also, to have more tunability, a series of pin headers are connected in parallel to the lossy side, where extra capacitors and resistors could be connected in parallel, as mentioned in Appendix B. The circuit is designed to work at the EPD frequency of $f_e = 988.6$ kHz, and indeed after tuning the circuit, we experimentally obtain an experimental EPD frequency at $f = 989.6$ kHz as shown in Fig. 7 with a green triangle at $C_2 = C_e$, very close to the designed
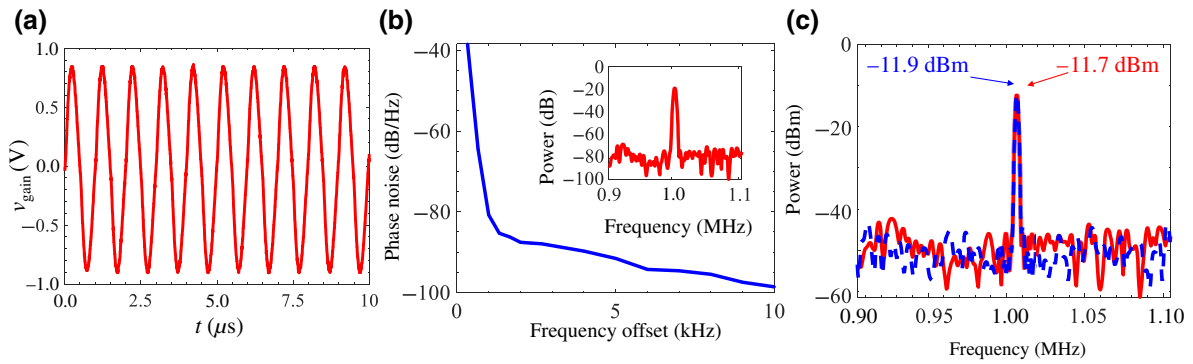
FIG. 8.   (a) Measured time-domain voltage signal at the capacitor C_1 using an oscilloscope, when the system is perturbed from EPD by $C_2 - C_e = 20$ pF, corresponding to a $\Delta_{C_2} = 0.013$. (b) Measured wideband spectrum by spectrum analyzer (Rigol DSA832E) signal analyzer as an inset with a fundamental frequency of oscillation of 1.002 MHz [theoretical expectation based on $\det(\mathbf{M} - j\omega\mathbf{I}) = 0$ is at 1.004 MHz]. Phase noise of the power spectrum is measured by the spectrum analyzer at frequency offsets from a few Hz to 10 kHz. The resolution bandwidth is set to 300 Hz, while video bandwidth is set to 30 Hz to fully capture the spectrum. (c) Measured power spectrum corresponding to a perturbation $\Delta_{C_2} = 0.013$ applied to C_2, using two different gain values: the red curve is based on gain of the EPD, and the blue curve is based on a gain that is around 1% larger than the EPD value.

one. The oscillation frequency is obtained by taking the FFT of the experimentally obtained time-domain voltage signal of the capacitor C_1 using an oscilloscope (Agilent Technologies DSO-X 2024A) after the signal reaches saturation for a time window of 10^2 periods with 10^6 points. The obtained oscillation frequency is in agreement with the result read directly on the spectrum analyzer (Rigol, model DSA832E).

We then perturb C_2 as $(1 + \Delta_{C_2})C_e$ where C_e satisfies the EPD condition, with small steps Δ_{C_2} as explained in Appendix B. As shown in Fig. 7, the measured oscillation frequency dramatically shifts away from the EPD frequency, following the trend of square root of Δ_{C_2} as theoretically predicted by Eq. (14) for the linear-gain case. The experimental results (green triangles) in Fig. 7 demonstrate that even for a small positive and negative perturbation $C_2 - C_e = \pm20$ pF, corresponding to a $\Delta_{C_2} = \pm0.013$, the oscillation frequency significantly changes, which can be easily detected even in practical noisy electronic systems. Figure 8(a) shows the experimental time-domain voltage signal of the capacitor C_1 with respect to the ground, when a relative perturbation $\Delta_{C_2} = 0.013$ is applied to C_2, measured by an oscilloscope. The spectrum's frequency is now measured with a spectrum analyzer, and shown in Fig. 8(b) as an inset. The frequency of the spectrum matches the perturbed ($\Delta_{C_2} = 0.013$) oscillation frequency, green triangle in Fig. 7, obtained from the Fourier transform of the time-domain experimental data. These results confirm that the structure is oscillating at the predicted perturbed resonance condition after saturation.

An essential feature of any oscillator is its ability to produce a near-perfect periodic time-domain signal (pure sinusoidal wave), and this feature is quantified in terms of phase noise, determined here based on the measured power spectrum up to 10-kHz frequency offset. The phase noise

and power spectrum in Fig. 8(b) demonstrate that electronic noise (which is significant in opamp) and thermal noise in the proposed highly sensitive oscillator scheme does not discredit the potential of this circuit to exhibit measurable high sensitivity to perturbations. Indeed, the low phase noise of -80.8 dB/Hz at 1-kHz offset from the oscillation frequency shows that the frequency shifts observed in Fig. 7 are well measurable. Note that this result is similar to the nonlinear saturation regime commonly observed in oscillators. The resonance oscillation peaks have a very narrow bandwidth (linewidth), which makes the oscillation frequency shifts very distinguishable and easily readable.

In the experiment, a relative perturbation $\Delta_{C_2} = 0.013$ (i.e., 1.3%) applied to C_2 leads to a frequency shift $\Delta f_{\Delta_{C_2}} = 1002$ kHz $- 989.6$ kHz $= 12.4$ kHz, which is much larger than the 1-kHz offset associated to -80.8-dB/Hz noise. The measured -3-dB (half power) spectral linewidth in the inset of Fig. 8(b) is equal to 0.8 kHz (using a resolution bandwidth of 300 Hz, and a video bandwidth of 30 Hz) that is much narrower than the measured frequency shift $\Delta f_{\Delta_{C_2}} = 12.4$ kHz.

In this oscillator-sensor system, we also have some freedom in choosing the small-signal gain value because the dynamics are also determined by the saturation arising from the nonlinear gain behavior. For example, in the experiment, we verify that circuit has the same oscillation frequency when using an unbalanced small-signal gain 1% larger than the balanced loss value. Figure 8(c) shows two measured frequency spectra corresponding to a relative perturbation $\Delta_{C_2} = 0.013$ applied to C_2, using two different gain values. The spectrum is measured using a resolution bandwidth of 300 Hz, while the video bandwidth is set to 30 Hz to fully capture the spectrum. The red curve is for the case with gain around 1% larger than

the balanced loss whereas the blue curve is for the case where gain and loss are balanced. These two frequency responses show the same oscillation frequency, with a very small difference in the power spectrum peak, which is 0.2 dBm higher for the case with 1% larger gain, as shown in Fig. 8(c). This feature helps us design the circuit without a very accurate balance between gain and loss, i.e., oscillator sensors can be realized without satisfying exactly *PT* symmetry (assuming the the sensing perturbation is not applied yet). As mentioned earlier, the nonlinear oscillator with broken *PT* symmetry exhibits the very useful feature that the oscillation frequency shifts are both positive and negative, depending on the sign of the perturbations Δ_{C_2}, hence *allowing for sensing both positive and negative* values of Δ_{C_2}. Note that the oscillator-sensing scheme is achieved without tuning the capacitance in the active part to keep the symmetry (to avoid instability), as it is instead done in a previous scheme using a *PT*-symmetric circuit [48].

VI. CONCLUSIONS

We demonstrate that two coupled *LC* resonators terminated with nonlinear gain, with almost balanced loss and small-signal gain, working near an EPD, make an oscillator whose oscillation frequency is very sensitive to perturbations. The nonlinear behavior of the active component is essential for the three features observed by simulations and experimentally: (i) the oscillation frequency is very sensitive to perturbations, and both positive and negative perturbations of a capacitor are measured, leading to very high sensitivity based on shifted oscillation frequency that approximately follows the square-root law, which is a property of EPD systems; (ii) the measured spectrum has very low phase noise allowing clean measurements of the shifted oscillation frequencies. (iii) It is not necessary to have a perfect gain and loss balance, i.e., we show that slightly broken gain and loss balance leads to the same results as for the case of perfectly balanced gain and loss.

Note that none of the features above are available in current *PT*-symmetry circuits in the literature [23,48]: Indeed, only one sign of the perturbation is measurable with the *PT*-symmetry circuits published so far, since the other sign leads to the circuit instability. Furthermore, to make a single sign perturbation measurement, in the literature, e.g., Ref. [48], the capacitor C_1 on the gain side has been tuned using a varactor to reach the value of the perturbed capacitor (C_2) on the reading side in order to rebuild the *PT* symmetry (but in a sensor operation it is not possible to know *a priori* the value that has to be measured); furthermore, to work at or very close to an EPD, using linear gain, the gain has to be set equal to the loss [balanced gain and loss condition].

The oscillation frequency shift follows the square-root-like behavior predicted by the Puiseux series expansion,
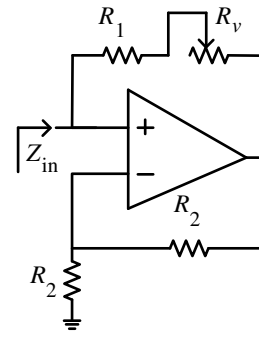
FIG. 9. Negative resistance converter circuit implementation by using an opamp.

as expected for EPD-based systems. We show the performance of the oscillator-sensor scheme based on two configurations: wireless coupling with a mutual inductor, and wired coupling by a capacitor. The latter oscillator scheme is fabricated and tested. We analyze how the nonlinearity in the gain element makes the circuit unstable and oscillate after reaching saturation. The oscillator's characteristics are determined in terms of transient behavior and sensitivity to perturbations due to either capacitance or resistance change in the system. The experimental verification provided results in very good agreement with theoretical expectations. The measured high sensitivity of the oscillator sensor to perturbations can be used as a practical solution for enhancing sensitivity, also because the measured shifted frequencies are well visible with respect to underlying noise. The proposed EPD-based oscillator sensor can be used in many automotive, medical, and industrial applications where detections of small variations of physical, chemical, or biological variations need to be detected.

APPENDIX A: NEGATIVE RESISTANCE

Several different approaches provide negative nonlinear conductance needed for proposed circuits. In this subsection, we show the circuit in Fig. 9 that utilizes opamp to achieve negative impedance. The converter circuit converts the impedance as $Z_{in} = -R_1$ while we design the circuit to work at the EPD point by choosing $R_1 = 1/G_e$. In the experiment, we use $R_1 = 100 \ \Omega$, and $R_2 = 2 \ k\Omega$ to achieve the EPD value. We tune the negative resistance with resistor trimmer R_v to reach the EPD value $G_e = 9$ ms.

APPENDIX B: IMPLEMENTATION OF THE NONLINEAR COUPLED OSCILLATOR

We investigate resonances and their degeneracy in the two LC resonators coupled by a capacitor as in Fig. 10(a), whereas Figs. 10(b) and 10(c) illustrate the PCB layout and assembled circuit. In the fabricated circuit, the sensing capacitance is shown in the red dashed box, the nonlinear gain is in the orange dashed box, and the dc supply is in the yellow dashed box. Inductors have values $L_1 = L_2 = 10 \ \mu$H, the loss value is set to $G_2 = 9$ mS with a linear resistor, the capacitor on the gain side and the coupling capacitor are $C_1 = C_c = 1.5$ nF. The gain element is designed with an opamp (Analog Devices Inc., model ADA4817), where the desired value of gain is achieved with a variable resistor RV1. In the experiment, we setup the nonlinear gain to be a bit larger (around 0.1%) than the balanced gain by tuning the RV1 to make the system slightly unstable. To tune and find the exact value of the

capacitance that leads to an EPD ($C_2 = C_e$), a variable capacitor (Sprague-Goodman, model GMC40300) and a series of pin headers, where extra capacitors could be connected in parallel to C_2, are provided. By adding small and known capacitor values on the load side, we tune the capacitance C_2 to bring the circuit very close to the EPD and observe the EPD oscillation frequency $f = f_e$.

To show the square-root-like behavior of the oscillator's frequency due to perturbations in Figs. 6 and 7, we perturb the capacitor C_2 with pairs of extra 10-pF capacitors to make 20-pF steps, connected in parallel to C_2, using the pin headers shown in Fig. 10. After each perturbation, the oscillation frequency is measured with an oscilloscope and also with a spectrum analyzer (for comparison and verification purposes), as discussed in Sec. B, and shown in Fig. 7 with green triangles. Moreover, for the perturbed circuit, considering $\Delta_{C_2} = 0.013$ applied to C_2 (any perturbed point can be chosen), we change the variable resistor RV1 to study oscillation frequency variation for different unbalanced nonlinear gains. The goal is to show that the circuit using a bit unbalancednonlinear gain still has the same oscillation frequency. Indeed, by trimming the RV1, we verify the same oscillation frequency for roughly 1% unbalanced gain and loss, as shown in Fig. 8(c). Note that on the PCB, the ground plane (on the bottom layer) is designed to connect all the ground of the measurement equipments and dc supply to the circuit's ground.

FIG. 10. (a) Schematic of the two LC resonators coupled by $C_c = 1.5$ nF with inductor $L_1 = L_2 = 10 \ \mu$H, the opamp U_1 (Analog Devices Inc., model ADA4817), the variable resistance RV$_1$ (Bourns Inc., model 3252W-1-501LF) and variable capacitance V_{C2} (Sprague-Goodman, model GMC40300), biasing capacitors $C_4 = C_6 = 0.1 \ \mu$F $C_5 = C_6 = 10 \ \mu$F as datasheet suggested. (b) PCB layout of the assembled circuit where the top layer traces are red, the ground plane and bottom traces are green, and the connecting vias are orange. In this design, via J1 is a probe point for the capacitor voltage, whereas vias J6 and J4 are test points connected to the ground plane and are used to connect the ground of the measurement equipment to the ground of the circuit. All the ground nodes are connected to the bottom green layer.

[1] B. Razavi, *Rf Microelectronics* (Prentice Hall, New Jersey, 1998), Vol. 206.

[2] B. V. der Pol, The nonlinear theory of electric oscillations, Proc. IRE **22**, 1051 (1934).

[3] G. W. Pierce, Piezoelectric crystal resonators and crystal oscillators applied to the precision calibration of wavemeters, Am. Acad. Arts Sci. **59**, 81 (1923).

[4] E. H. Colpitts, Oscillation generator, Google Patents, 1927.

[5] H. Wu and A. Hajimiri, Silicon-based distributed voltage-controlled oscillators, IEEE J. Solid-State Circuits **36**, 493 (2001).

[6] H.-A. Tanaka, A. Hasegawa, H. Mizuno, and T. Endo, Synchronizability of distributed clock oscillators, IEEE Trans. Circuits Syst. I: Fundam. Theory Appl. **49**, 1271 (2002).

[7] D. Oshmarin, A. F. Abdelshafy, A. Nikzamir, M. M. Green, and F. Capolino, Experimental demonstration of a new oscillator concept based on degenerate band edge in microstrip circuit, Preprint arXiv:2109.07002.

[8] A. Hajimiri, S. Limotyrakis, and T. Lee, Jitter and phase noise in ring oscillators, IEEE J. Solid-State Circuits **34**, 790 (1999).

[9] R. Nayak, I. Kianpoor, and P. G. Bahubalindruni, Low power ring oscillator for IoT applications, Analog Integr. Circuits Signal Process. **93**, 257 (2017).

[10] H.-C. Chang, X. Cao, U. Mishra, and R. York, Phase noise in coupled oscillators: Theory and experiment, IEEE Trans. Microw. Theory Tech. **45**, 604 (1997).

[11] T. Endo and S. Mori, Mode analysis of a multimode ladder oscillator, IEEE Trans. Circuits Syst. **23,** 100 (1976).

[12] W. D. Heiss and A. L. Sannino, Avoided level crossing and exceptional points, J. Phys. A: Math. Gen. **23,** 1167 (1990).

[13] M. I. Vishik and L. A. Lyusternik, The solution of some perturbation problems for matrices and selfadjoint or non-selfadjoint differential equations I, Russ. Math. Surv. **15,** 1 (1960).

[14] A. P. Seyranian, Sensitivity analysis of multiple eigenvalues, J. Struct. Mech. **21,** 261 (1993).

[15] P. Lancaster, On eigenvalues of matrices dependent on a parameter, Numer. Math. **6,** 377 (1964).

[16] T. Kato, *Perturbation Theory for Linear Operators* (Springer-Verlag New York Inc., New York, 1966).

[17] C. M. Bender, M. V. Berry, and A. Mandilara, Generalized PT symmetry and real spectra, J. Phys. A: Math. Gen. **35,** L467 (2002).

[18] W. D. Heiss, The physics of exceptional points, J. Phys. A Math. Theor. **45,** 444016 (2012).

[19] B. Peng, Ş. K. Özdemir, F. Lei, F. Monifi, M. Gianfreda, G. L. Long, S. Fan, F. Nori, C. M. Bender, and L. Yang, Parity–time-symmetric whispering-gallery microcavities, Nat. Phys. **10,** 394 (2014).

[20] A. P. Seyranian, O. N. Kirillov, and A. A. Mailybaev, Coupling of eigenvalues of complex matrices at diabolic and exceptional points, J. Phys. A: Math. Gen. **38,** 1723 (2005).

[21] M. Berry, Physics of nonhermitian degeneracies, Czech. J. Phys. **54,** 1039 (2004).

[22] T. Stehmann, W. D. Heiss, and F. G. Scholtz, Observation of exceptional points in electronic circuits, J. Phys. A: Math. Gen. **37,** 7813 (2004).

[23] J. Schindler, A. Li, M. C. Zheng, F. M. Ellis, and T. Kottos, Experimental study of active LRC circuits with $\mathcal{PT}$ symmetries, Phys. Rev. A **84,** 040101(R) (2011).

[24] M. Sakhdari, M. Farhat, and P.-Y. Chen, PT-symmetric metasurfaces: Wave manipulation and sensing using singular points, New J. Phys. **19,** 065002 (2017).

[25] K. Rouhi, A. Nikzamir, A. Figotin, and F. Capolino, Exceptional point in a degenerate system made of a gyrator and two unstable resonators, Phys. Rev. A **105,** 032214 (2022).

[26] A. Nikzamir, K. Rouhi, A. Figotin, and F. Capolino, How to achieve exceptional points in coupled resonators using a gyrator or PT-symmetry, and in a time-modulated single resonator: High sensitivity to perturbations, EPJ Appl. Metamater. **9,** 14 (2022).

[27] H. Kazemi, A. Nikzamir, T. Mealy, A. Abdelshafy, and F. Capolino, High-sensitive parity-time symmetric oscillator in coupled transmission lines with nonlinear gain, IEEE J. Microw. **2,** 389 (2022).

[28] H. Hodaei, M.-A. Miri, M. Heinrich, D. N. Christodoulides, and M. Khajavikhan, Parity-time-symmetric microring lasers, Science **346,** 975 (2014).

[29] A. Figotin and I. Vitebskiy, Gigantic transmission band-edge resonance in periodic stacks of anisotropic layers, Phys. Rev. E **72,** 036619 (2005).

[30] M. A. K. Othman and F. Capolino, Theory of exceptional points of degeneracy in uniform coupled waveguides and balance of gain and loss, IEEE Trans. Antennas Propag. **65,** 5289 (2017).

[31] J. T. Sloan, M. A. K. Othman, and F. Capolino, Theory of double ladder lumped circuits with degenerate band edge, IEEE Trans. Circuits Syst. Regul. Pap. **65,** 3 (2018).

[32] A. F. Abdelshafy, M. A. K. Othman, D. Oshmarin, A. T. Almutawa, and F. Capolino, Exceptional points of degeneracy in periodic coupled waveguides and the interplay of gain and radiation loss: Theoretical and experimental demonstration, IEEE Trans. Antennas Propag. **67,** 6909 (2019).

[33] T. Mealy and F. Capolino, General conditions to realize exceptional points of degeneracy in two uniform coupled transmission lines, IEEE Trans. Microw. Theory Tech. **68,** 3342 (2020).

[34] S. Klaiman, U. Günther, and N. Moiseyev, Visualization of Branch Points in $\mathcal{PT}$-Symmetric Waveguides, Phys. Rev. Lett. **101,** 080402 (2008).

[35] C. E. Rüter, K. G. Makris, R. El-Ganainy, D. N. Christodoulides, M. Segev, and D. Kip, Observation of parity–time symmetry in optics, Nat. Phys. **6,** 192 (2010).

[36] J. Schnabel, H. Cartarius, J. Main, G. Wunner, and W. D. Heiss, $\mathcal{PT}$-symmetric waveguide system with evidence of a third-order exceptional point, Phys. Rev. A **95,** 053868 (2017).

[37] H. Kazemi, M. Y. Nada, T. Mealy, A. F. Abdelshafy, and F. Capolino, Exceptional Points of Degeneracy Induced by Linear Time-Periodic Variation, Phys. Rev. Appl. **11,** 014007 (2019).

[38] H. Kazemi, M. Y. Nada, A. Nikzamir, F. Maddaleno, and F. Capolino, Experimental demonstration of exceptional points of degeneracy in linear time periodic systems and exceptional sensitivity, J. Appl. Phys. **131,** 144502 (2022).

[39] H. Kazemi, A. Hajiaghajani, M. Y. Nada, M. Dautta, M. Alshetaiwi, P. Tseng, and F. Capolino, Ultra-sensitive radio frequency biosensor at an exceptional point of degeneracy induced by time modulation, IEEE Sens. J. **21,** 7250 (2021).

[40] M. Y. Nada, M. A. K. Othman, and F. Capolino, Theory of coupled resonator optical waveguides exhibiting high-order exceptional points of degeneracy, Phys. Rev. B **96,** 184304 (2017).

[41] M. A. K. Othman, F. Yazdi, A. Figotin, and F. Capolino, Giant gain enhancement in photonic crystals with a degenerate band edge, Phys. Rev. B **93,** 024301 (2016).

[42] A. Figotin and I. Vitebskiy, Oblique frozen modes in periodic layered media, Phys. Rev. E **68,** 036609 (2003).

[43] Y. Choi, C. Hahn, J. W. Yoon, and S. H. Song, Observation of an anti-PT-symmetric exceptional point and energy-difference conserving dynamics in electrical circuit resonators, Nat. Commun. **9,** 00 (2018).

[44] Z. Dong, Z. Li, F. Yang, C.-W. Qiu, and J. S. Ho, Sensitive readout of implantable microsensors using a wireless system locked to an exceptional point, Nat. Electron. **2,** 335 (2019).

[45] Z. Xiao, H. Li, T. Kottos, and A. Alù, Enhanced Sensing and Nondegraded Thermal Noise Performance Based on $\mathcal{PT}$-Symmetric Electronic Circuits with a Sixth-Order Exceptional Point, Phys. Rev. Lett. **123,** 213901 (2019).

[46] C. Zeng, Y. Sun, G. Li, Y. Li, H. Jiang, Y. Yang, and H. Chen, Enhanced sensitivity at high-order exceptional

points in a passive wireless sensing system, Opt. Express **27**, 27562 (2019).

[47] C. M. Bender and S. Boettcher, Real Spectra in Non-Hermitian Hamiltonians having PT Symmetry, Phys. Rev. Lett. **80**, 5243 (1998).

[48] P.-Y. Chen, M. Sakhdari, M. Hajizadegan, Q. Cui, M. M.-C. Cheng, R. El-Ganainy, and A. Alù, Generalized parity–time symmetry condition for enhanced sensor telemetry, Nat. Electron. **1**, 297 (2018).

[49] W. D. Heiss, Exceptional points of non-Hermitian operators, J. Phys. A: Math. Gen. **37**, 2455 (2004).

[50] J. Wiersig, Robustness of exceptional-point-based sensors against parametric noise: The role of Hamiltonian and Liouvillian degeneracies, Phys. Rev. A **101**, 053846 (2020).

[51] S. Kananian, G. Alexopoulos, and A. S. Poon, Coupling-Independent Real-Time Wireless Resistive Sensing through Nonlinear $\mathcal{PT}$ Symmetry, Phys. Rev. Appl. **14**, 064072 (2020).

[52] O. Kotlicki, J. Scheuer, and M. Shahriar, Theoretical study on Brillouin fiber laser sensor based on white light cavity, Opt. Express **20**, 28234 (2012).

[53] J. Scheuer, White light cavity formation and superluminal lasing near exceptional points, Opt. Express **26**, 32091 (2018).

[54] A. Welters, On explicit recursive formulas in the spectral perturbation analysis of a Jordan block, SIAM J. Matrix Anal. Appl. **32**, 1 (2011).

[55] K. Scharnhorst, Angles in complex vector spaces, Acta Appl. Math. **69**, 95 (2001).